Scripta Materialia 203 (2021) 114113

Contents lists available at ScienceDirect

Scripta Materialia

journal homepage: www.elsevier.com/locate/scriptamat

Improved mechanical properties of cast Mg alloy welds via texture weakening by differential rotation refill friction stir spot welding

Banglong Fu[a,*], Junjun Shen[a,*], Uceu F.H.R. Suhuddin[a], Ting Chen[a], Jorge F. dos Santos[a], Benjamin Klusemann[a,b], Michael Rethmeier[c,d]

[a] Helmholtz-Zentrum Hereon, Institute of Material Mechanics, Solid State Materials Processing, Max-Planck-Str. 1, Geesthacht 21502, Germany
[b] Leuphana University of Lüneburg, Institute of Product and Process Innovation, Universitätsallee 1, Lüneburg 21335, Germany
[c] Technical University Berlin, Institute for Machine Tools and Factory Management (IWF), Pascalstr. 8-9, Berlin 10587, Germany
[d] BAM Bundesanstalt für Materialforschung und -prüfung, Unter den Eichen 87, Berlin 12205, Germany

ARTICLE INFO

Article history:
Received 7 May 2021
Revised 18 June 2021
Accepted 22 June 2021

Editor: Greg Rohrer

Keywords:
Refill friction stir spot welding
Magnesium alloy
Texture
EBSD
Plastic deformation

ABSTRACT

Cast magnesium alloys welds produced by refill friction stir spot welding (refill FSSW) show low lap shear strength (LSS) and constantly fail in stirred zone (SZ) shear mode. The cause is most probably related to the heavily textured microstructure. Here, to re-engineer the resulting microstructure, we propose a novel process variant, the differential rotation refill FSSW (DR-refill FSSW). DR-refill FSSW stimulates discontinuous dynamic recrystallization and produces a bimodal microstructure with weakened texture. Therefore, the deformation incompatibility between SZ and thermal-mechanically affected zone is avoided. The welds have 50% higher LSS than that of standard refill FSSW welds, and fail in a different failure mode, i.e., SZ pull-out mode. DR-refill FSSW provides a new and effective strategy for improving the performance of spot welds based on microstructural engineering.

While the compelling need for lightweight, energy-efficient, environmental friendly engineering systems has motivated the use of magnesium (Mg) alloys [1], its application in the automotive industry is still limited due to challenges associated with manufacturing, processing, and in-service performance [2,3]. In particular, appropriate welding processes need to be developed to widen the structural application range of Mg alloys. Solid-state welding techniques are especially efficient due to avoidance of serious metallurgical problems as porosity and hot cracking, which are often present in conventional fusion based welding processes [4,5].

During the past few years, a relatively new solid-state spot welding process, refill friction stir spot welding (refill FSSW), has attracted much attention due to the advantages of a keyhole-free surface, sound mechanical properties and no need for additional filler material [6,7]. It has been successfully used mainly for welding aluminum (Al) based similar and dissimilar combinations [8–11]. In contrast, studies concerning Mg alloys are limited [12,13]. Although Mg alloys produced by casting processes represent 98% of Mg usage [14], no work has been reported on refill FSSW of cast Mg alloy in the literature.

Preliminary unpublished studies on refill FSSW of cast Mg alloys consistently revealed low lap shear strength (LSS) of the welds, failing in stirred zone (SZ) “shear” mode, regardless of the process parameters used. It is well known that the texture is strongly connected to the mechanical properties of Mg alloys due to its hexagonal close-packed (hcp) crystal structure, which offers only limited independent slip systems and shortage of accommodating deformation along the <*c*>-axis [15,16]. Refill FSSW is characterized by a layered material flow behavior driven by simple shear and extrusion [8], thus the development of strong crystallographic texture is expected. Indeed, in friction stir welding/processing (FSW/P) of Mg alloys, the formation of sharp basal texture with inhomogeneous distribution has been reported [17]. This favors activation of basal slip and extension twinning adjacent to the SZ edge while slip/twinning in the SZ center during transverse tensile tests is inhibited [18], leading to severe strain localization and deteriorated mechanical properties. Through post-deformation/aging [19], multi-pass FSW/P [20], asymmetrical double-sided FSW [21], the basal texture could be weakened/randomized, and the mechanical performance was improved. The benefits of texture weakening of Mg alloys for the overall mechanical response, i.e. improved formability/ductility, decreased anisotropy, have also been reported in rolling of Mg alloys, by microalloying with other elements [22,23] and imposing severe

* Corresponding author.
E-mail addresses: banglong.fu@hereon.de (B. Fu), junjun.shen@hereon.de (J. Shen).

https://doi.org/10.1016/j.scriptamat.2021.114113

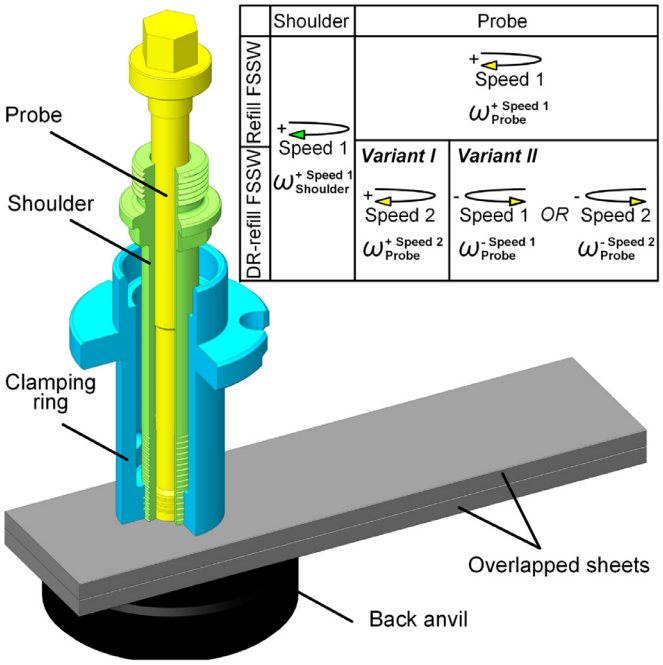

Fig. 1. Schematic illustration of refill FSSW and DR-refill FSSW process.

plastic deformation through asymmetric rolling [24] or high strain-rate rolling [25]. Therefore, to achieve a sound refill FSSW Mg alloys weld with superior mechanical properties, the texture intensity needs to be reduced.

The present study aims at introducing a novel refill FSSW process variant, named "*differential rotation refill FSSW (DR-refill FSSW)*", which produces spot welds in Mg alloys with improved LSS compared to conventional refill FSSW, through texture weakening. Fig. 1 presents a schematic view of both processes and highlights the differences between refill FSSW and DR-refill FSSW. A more detailed description of tool movement and rotation is provided in Supplementary **Fig. S1**. A three-piece tool system, consisting of a clamping ring (diameter of 15 mm), a shoulder (9 mm) and a probe (6 mm), is used. Although the translational tool movement between refill FSSW and DR-refill FSSW is the same, the rotation state is different. To simplify the expression, the nomenclature of rotation state is defined as: $\omega^{+/-\ Speed}_{Shoulder/Probe}$, which includes the considered tool parts, i.e. shoulder or probe, rotation direction ("+" denotes the clockwise direction) and speed in rpm. Unlike refill FSSW, in which probe and shoulder share the same rotation direction and speed, in DR-refill FSSW, these are different. Depending on the rotation direction, two DR-refill FSSW variants are possible: (I) probe and shoulder rotate in the same direction, but the rotation speed is different; (II) probe and shoulder rotate in opposite directions with the same or different rotation speeds.

The base material (BM) selected for this study was Mg alloy AM50-F (Mg-5.2Al-0.5Mn-0.05Zn-0.03Si, in wt.%) with an average grain size of 1.8 mm, produced by permanent mold direct chill casting [26]. The original cast ingot was sectioned into target sheets measuring 100 (L) × 25.4 (W) × 3 (T) mm^3. The sheets were positioned in lap configuration with an overlap distance of 25.4 mm before welding. The special-purpose welding machine RPS 200, produced by Harms & Wende, was used to perform the welding. The employed welding parameters are summarized in Table 1. The cross-sections of the welds were polished and color-etched with acetic-picral etchant. The etched samples were examined by a LEICA DM-IRM optical microscope with polarized light plus sensitive tint to reveal the colored grains. The global macrotexture of the SZ was obtained by synchrotron radiation at Deutsches Elektronen-Synchrotron (DESY). A monochromatic X-ray beam with the energy of 87 keV and size of 1.0 × 1.0 mm^2 was used and the extracted SZ was examined in transmission mode. The pole figures (PFs) were determined using Fit2D [27] and in-house code package SABO according to steps developed by Yi et al. [28]. Detailed supporting information of measurement and calculation is provided in Supplementary **Fig. S2**. The local microtexture of selected positions in the SZ was determined by FEI Quanta 650 field-emission scanning electron microscope equipped with EDAX electron backscattered diffraction (EBSD) detector. EBSD data was acquired at 15 kV with a step size of 0.2 µm and analyzed via TSL OIM software. Room temperature LSS tests were performed via a Zwick/Roell universal testing machine at a crosshead speed of 1 mm/min. For completeness, the dimension of the LSS test sample and the used fixture system are illustrated in Supplementary **Fig. S3**. Three samples per welding condition were tested.

Fig. 2**(a)** summarizes the resulting LSS and fracture mode for different probe rotation states $\omega^{+/-}_{Probe}$. The surface morphology and cross-section of failed specimens are presented in Fig. 2**(b)**. Compared to welds obtained by refill FSSW $\omega^{+\ 1800}_{Probe}$, the DR-refill FSSW welds according to variant I, ω^{+}_{Probe}, reveal only a minor increase of the LSS, and the difference in rotation speeds is negligible. All these welds still fail in the shear mode. The cracks mainly propagate along the boundary between SZ and thermo-mechanically affected zone (TMAZ), then separating the upper and lower sheets throughout the SZ. However, when the rotation directions of shoulder and probe are opposite, i.e. variant II as ω^{-}_{Probe}, the LSS increases significantly, and nearly all produced welds fulfill the strength requirement of referred standard [29]. For these welds, when ω^{-}_{Probe} is higher than $\omega^{+\ 1800}_{Shoulder}$, i.e. $\omega^{-\ 2400}_{Probe}$ and $\omega^{-\ 3000}_{Probe}$, during LSS test, the circular cracks mainly grow along the SZ edge and finally close on the upper sheet surface, thus the SZ remains entirely on the lower sheet, resulting in a different failure mode: SZ "pull-out" mode.

The results of LSS illustrate that the DR-refill FSSW with opposite rotation directions of probe and shoulder has evident advantages for the welding of cast Mg alloys. To reveal the underlying mechanism of this performance improvement, welds obtained by refill FSSW with $\omega^{+\ 1800}_{Probe}$ (weld-A), DR-refill FSSW with $\omega^{-\ 1800}_{Probe}$ (weld-B) and $\omega^{-\ 3000}_{Probe}$ (weld-C), were investigated in detail. The cross-sectional micrographs are shown in Fig. 2**(c)**. All three welds display defect-free macrostructures, where no voids or lack-of-refill are observed. The coloration of grains under polarized light is related to birefringence induced by anisotropic film deposition during etching, which varies according to crystallographic orientation of the underlying grains [30]. In contrast to the probe refill region of the SZ in weld-A, which is characterized by a nearly uniform region, the corresponding regions of weld-B and C can be subdivided into two subregions. The newly formed upper subregion is deduced to be related to the reverse rotation of the probe. In the lower subregion, weld-B and C display the heterogeneous color patterns, implying possible great difference in orientation, which usually means the underlying dilute integral texture development. Thus, the texture patterns were investigated to verify the hypothesis that texture was weakened in weld-B and C compared to weld-A.

The initial texture of AM50 Mg alloy BM was first examined, and the obtained (0002) basal and $(10\bar{1}0)$ prismatic plane PFs are shown in Fig. 3**(a)**. The as-cast BM exhibits a near-random texture with the maximal basal pole intensity I_{max} of 6.2 in multiple random distribution. The recalculated (0002) and $(10\bar{1}0)$ PFs of the SZ of welds A-C are shown in Fig. 3**(b)**. After welding, according to the (0002) PF of weld-A, a "basal" texture with symmetrical spread of basal plane normal (<*c*>-axis) by ± 35° maximum from ND toward TD-LD plane is formed. Since the {0002} plane tends to rotate around the <*c*>-axis randomly, the corresponding $(10\bar{1}0)$ PF

Table 1
DR-refill FSSW parameters range (likewise, "+" means rotation direction is clockwise, see Fig. 1). The rotation state of the probe varied, while that of shoulder was fixed at $\omega_{Shoulder}^{+\ 1800}$, i.e. clockwise at 1800 rpm.

Rotation state (rpm)		Welding time (s)			Plunge depth (mm)
Shoulder	Probe *	Plunge time	Dwell time	Retraction time	
$\omega_{Shoulder}^{+\ 1800}$	$\omega_{Probe}^{+/-\ (600-3000)}$	2	1	2	3

* Note when the probe rotates in $\omega_{Probe}^{+\ 1800}$, the weld is obtained by conventional refill-FSSW.

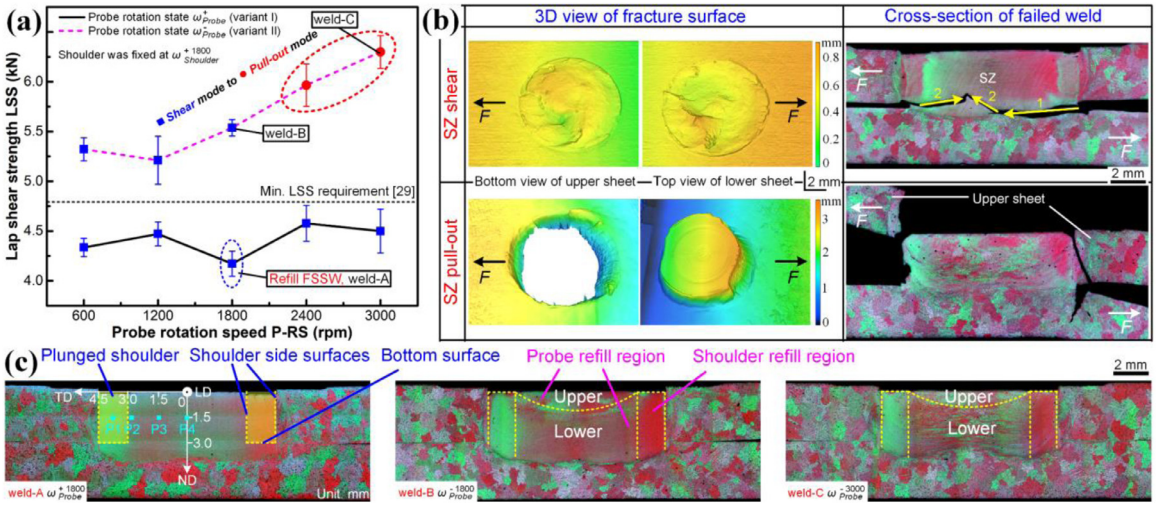

Fig. 2. (a) LSS and fracture mode for different probe rotation states, the shoulder rotation state is fixed at $\omega_{Shoulder}^{+\ 1800}$, thus ω_{Probe}^{+} and ω_{Probe}^{-} correspond to the variant I and II of DR-refill FSSW, respectively. (b) Illustrations of failure modes: SZ shear and pull-out mode. (c) Cross-sectional macrostructures of weld-A, B and C. The experimental coordinate system is defined by normal direction (ND), transverse direction (TD) and longitudinal direction (LD) as shown in (c).

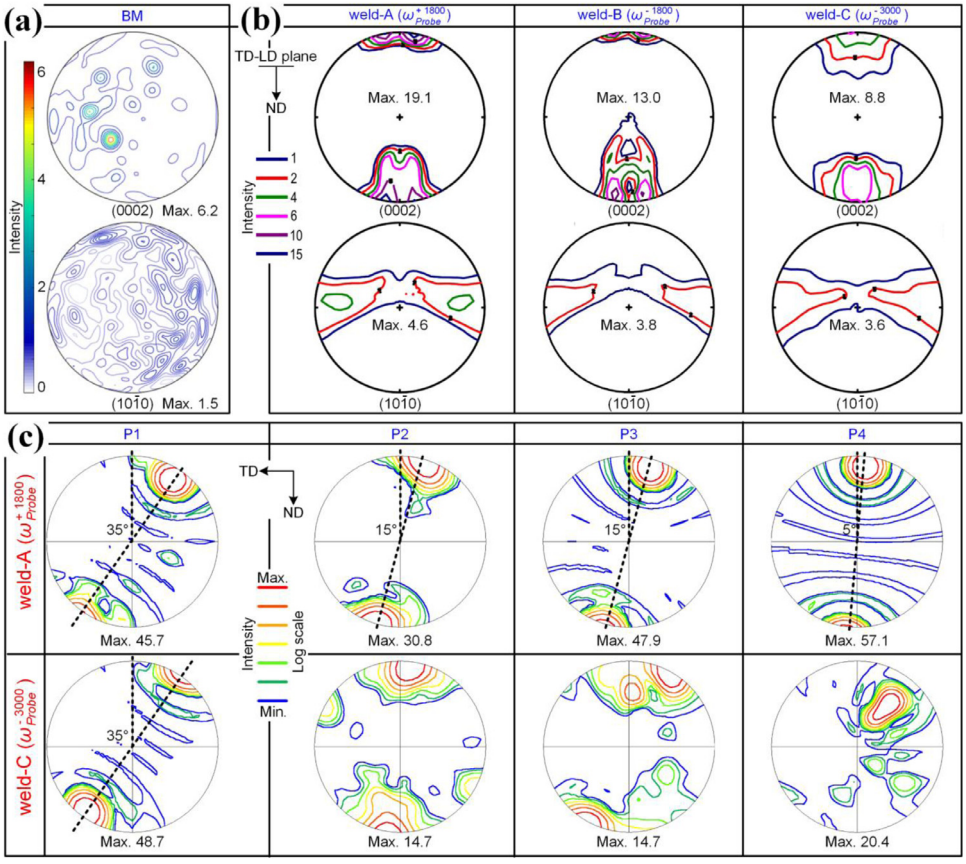

Fig. 3. The (0002) and (10$\bar{1}$0) PFs showing macrotexture of (a) BM and (b) SZ of weld-A, B and C. (c) (0002) PF of P1-4 positions illustrated in Fig. 2(c). Note that the initial macrotexture of BM was examined by X-ray diffraction. To obtain grain statistics, an area of 100 × 50 mm^2 was scanned.

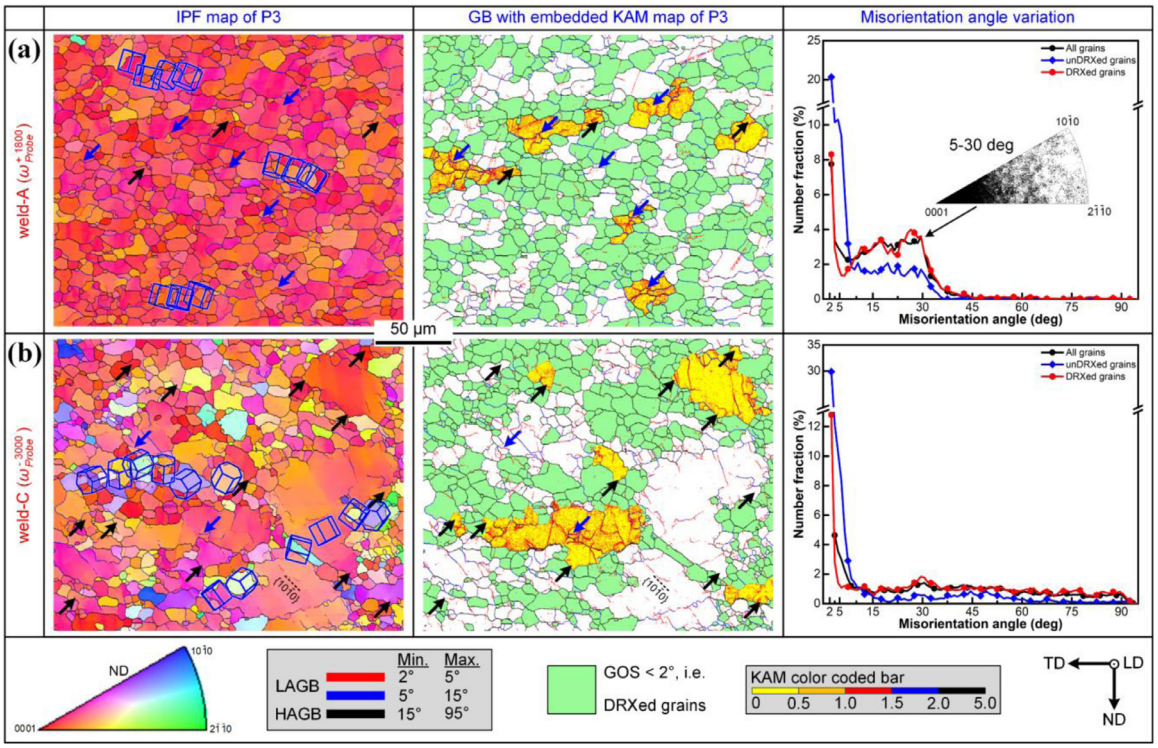

Fig. 4. EBSD analysis of microstructure at the position P3. (a) weld-A, (b) weld-C. The grain orientation spread (GOS) of 2° is the threshold value for DRXed (colored by green in GBs map) and unDRXed grains. The regions black arrowed illustrate DDRX, and those blue arrowed show CDRX. Some grains are highlighted by blue hcp crystal lattice to show the orientation intuitively.

indicates the development of a weak fiber texture without significant preferred orientation ($I_{max} < 5$). The texture patterns of weld-B and weld-C are similar to weld-A. However, the dominant basal texture is weakened, base pole intensity I_{max} decreases from 19.1 for weld-A to 13.0 of weld-B and 8.8 of weld-C.

To accurately reveal the texture difference, further insight into the local microtexture is necessary. Fig. 3**(c)** shows the (0002) PFs at positions P1-P4, indicated in Fig. 2**(c)**, for both weld-A and weld-C.

In case of weld-A, the evolved sharp basal texture ($I_{max} > 30$) is determined at all the investigated positions, which is consistent with the measured macrotexture. It is important to notice that, when approaching the SZ center, i.e. from P1 to P4, the basal plane tilt is characterized with "transitional" features. The exact orientation of the basal pole peak deviates gradually from TD towards ND with the decrease of <0002> inclined angle from 35° at P1 to 5° at P4, indicating the strengthening of the near-<0002>‖ND texture component. The reorientation of <0002> with positions P1-P4 reveals the development of typical {0002}<*uvtw*> B-fiber shear texture [31], in which the {0002} basal plane tends to align parallel to the macroscopic shear plane due to basal slip. The predominant material flow in refill FSSW can be generally described as simple shear, which is mainly driven by the rotation of the shoulder [8]. The plastically deformed material interacts simultaneously with both the side and bottom surfaces of the shoulder. Since the edge effect of the shoulder side surface decreases towards the SZ center, the combined macroscopic shear plane inclines gradually from the plane along shoulder side surface to that parallel to the bottom surface, giving rise to the location-dependency of basal pole tilt from P1 to P4 position. The P1 position of weld-C, which belongs to the shoulder refill region, shows a similar texture to weld-A. However, within the probe refill region (P2-P4), the basal texture is diminished, and the texture is significantly weakened/randomized with complicated pattern. For example, at P3, I_{max} is reduced from 47.9 of weld-A to 14.7 in weld-C. Additionally, no apparent regularity of texture variation is identified from P2 to P4 for weld-C, indicating a turbulent material flow within the probe refill region.

The above results clearly show that DR-refill FSSW at ω^{-}_{Probe}, i.e. probe and shoulder rotate in opposite direction, leads to substantial texture weakening compared to refill FSSW. Considering the LSS improvement and the different observed failure mode, see Fig. 2**(a)** and **(b)**, the benefits of "weakened texture" on the mechanical properties of cast Mg weld are revealed. The characteristic microstructural differences and their influence on the deformation behavior between standard refill FSSW and DR-refill FSSW are further discussed in the following to better understand the underlying mechanisms.

The microstructure at the representative position P3, which is within the probe refill region, see Fig. 2**(c)**, was analyzed via EBSD for weld-A and weld-C, see Figs. 4**(a)** and **(b)**. The extracted grain and texture information are summarized in Table 2.

For the weld-A, a continuous high-angle grain boundaries (HAGBs) perimeter cannot be observed. The grain morphology features an irregular mixture of low-angle grain boundaries (LAGBs) and HAGBs with prevalence of LAGBs and high HAGBs distance. Such microstructures have also been reported in FSW/P of Mg alloys [4,17,32,33], which are related to "grain convergence" [17] under the effect of strong texture development during severe plastic deformation. Additionally, the identified grain structure indicates the occurrence of dynamic recrystallization (DRX). The black arrowed positions of IPF and GBs maps show the DRXed grains originate from bulging of corrugated HAGBs. According to the embedded Kernel Average Misorientation (KAM) map, the local regions with low misorientation exist on the concave sides, thus strain-induced boundary migration [34,35] occurs, implying the activation of discontinuous dynamic recrystallization (DDRX). However, fine DRXed grains, blue arrowed, also form due to the gradual LAGB-to-HAGB transformation through dislocation rearrangement, which

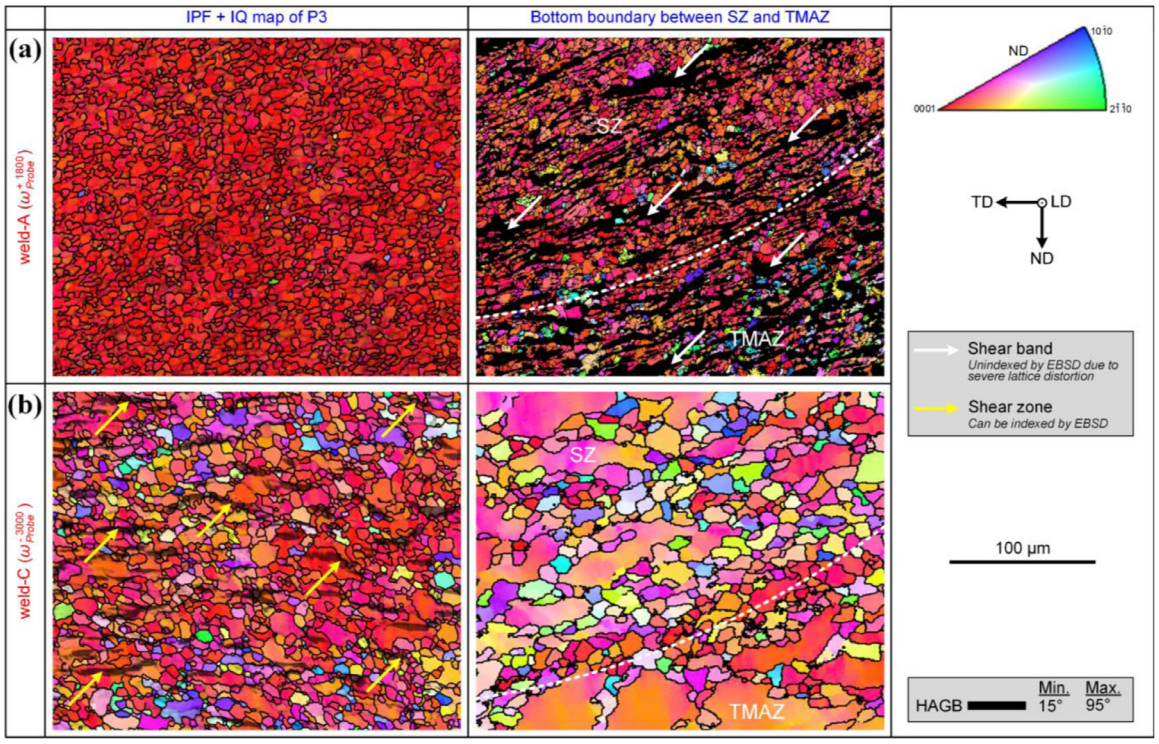

Fig. 5. EBSD analysis of microstructure at the position P3 and the bottom boundary between SZ and TMAZ after applying 4 kN force. (a) weld-A, (b) weld-C. The image quality (IQ) map overlapped with IPF shows the existence of shear zone, which can be indexed by EBSD, while the shear band cannot be indexed due to severe lattice distortion.

Table 2
Extracted grain and texture information according to EBSD for weld-A and weld-C at position P3 after welding (final weld) as well as after LSS test at 4 kN.

Weld	Grain information				Basal texture intensity		
	Size (μm)	HAGBs distance (μm)	LAGBs fraction (%)	DRX fraction (%)	Whole	unDRXed	DRXed
weld-A	7.6	16.2	36.9	58.6	47.9	53.2	44.1
weld-C	6.9	8.8	36.8	51.6	14.7	24.3	5.9
weld-A	4.6	18.2	43.8	58.3	69.6	75	65.7
weld-C	5.4	5.8	23.8	60	15.4	23.4	10.5

are related to continuous dynamic recrystallization (CDRX). The DRXed grains show a strong basal texture close to that of the unDRXed grains with rotation mainly along <0002>. Moreover, compared to the misorientation distribution of unDRXed grains, the fraction of LAGBs decreases while that of the range 15-30° preferentially increases in DRXed grains. Both results discussed above indicate that CDRX is the main contributor to recrystallization. It is important to point out that, for the SZ of weld-A, the misorientation distribution is somewhat unusual, the maximum misorientation is usually restricted below 30°, and the misorientation axes cluster near <0001> in the interval of 5-30°. This unique feature can be interpreted by the development of a strong B-fiber texture, which means that the grains are arbitrarily rotated along <0002>. The rotation angle above 30° is considered as equivalent due to the symmetry of the hcp crystal structure [4,17].

In weld-C, a bimodal grain morphology is identified. The necklaces of fine DRXed grains generally decorate the GBs of coarse unDRXed grains. It is clear that most DRXed grains have nucleated through bulging of GBs, and are completely surrounded by HAGBs without sub-structures. The crystallographic orientations of the DRXed grains are not close to the matrix as observed in weld-A but random, see the inserted hcp unit cells, thus the texture of DRXed grain is significant weakened (I_{max} = 5.9). These observations well document the primary recrystallization mechanism in weld-C to be DDRX [36–38], although some traces of CDRX are observed as well. Due to the weakened texture of weld-C, convergence of GBs disappears, and the HAGBs distance is smaller than that in weld-A. However, the fraction of LAGBs does not change, which is related to the development of geometrically necessary boundaries [39,40] within the unDRXed grain interiors. These boundaries are LAGBs in natural and straight in morphology with the traces close to $\{10\bar{1}0\}$ or $\{11\bar{2}0\}$ planes. The misorientation variation from unDRXed to DRXed grains is characterized with a homogeneous increase in the entire HAGBs range, which again indicates the dominant role of DDRX in weld-C.

The differences in microstructure between weld-A and C influence the deformation behavior during LSS, and finally result in varied failure modes. To reveal the underlying relationship, both welds were firstly loaded at 4 kN, i.e. near to the maximum LSS of weld-A, and then unloaded to analyze the microstructure. The EBSD results are shown in Fig. 5. The corresponding grain and texture information is also included in Table 2.

For the weld-A, the microstructure with a mixture of LAGBs and HAGBs still exists at position P3 of the SZ, see Fig. 5**(a)**. Compared to the original weld, after loading, both the LAGBs fraction and HAGBs distance increase, see Table 2, which are related to the further developments of dislocation interaction and grain convergence, indicating strain hardening within the SZ [33]. Thus, de-

formation incompatibility occurs along the boundary between SZ and TMAZ, leading to the formation of shear bands with severe lattice distortion and local strain, which are preferred sites of failure. While in weld-C, the deformation of the SZ is concentrated mainly along the GBs of fine and coarse grains, leading to further development of DRX and the formation of micro- shear zones, see Fig. 5**(d)**. These shear zones are short and discontinuous, which can accommodate strain by dislocation slip and repeated DRX [41,42]. The shear zones are distributed homogeneously within the whole SZ, providing a stabilizing effect between the deformation of SZ and TMAZ. Thus, the formation of shear bands is restrained, resulting in the SZ pull-out failure mode.

In summary, a novel welding variant, DR-refill FSSW, is reported, which can introduce a bimodal microstructure with weakened texture compared to conventional refill FSSW, leading to a significant increase in LSS of the weld in cast Mg alloy. Additionally, DR-refill FSSW has also shown competitive advantages in the welding of other materials combinations such as Al/Al, Mg/steel, which will be reported in the future.

Declaration of Competing Interest

The authors declare that they have no known competing financial interests or personal relationships that could have appeared to influence the work reported in this paper.

Acknowledgments

The authors are grateful to Prof. Dr. Norbert Hort at Helmholtz-Zentrum Hereon (HEREON) for providing the Mg alloy ingots. We acknowledge Deutsches Elektronen-Synchrotron DESY (Hamburg, Germany), a member of the Helmholtz Association HGF, for the provision of experimental facilities. Parts of the research were carried out at the High Energy Materials Science (HEMS) of HEREON and we would like to thank Dr. Xiaohua Zhou for assistance in using P07B beamline. We would also like to acknowledge to Dr. Sangbong Yi for training on SABO software. Banglong Fu gratefully acknowledges funding by China Scholarship Council (grant no. 201506220158).

Supplementary materials

Supplementary material associated with this article can be found, in the online version, at doi:10.1016/j.scriptamat.2021.114113.

References

[1] T.M. Pollock, Science 328 (2010) 986–987.
[2] W.J. Joost, P.E. Krajewski, Scr. Mater. 128 (2017) 107–112.
[3] B.C. Suh, M.S. Shim, K.S. Shin, N.J. Kim, Scr. Mater. 84–85 (2014) 1–6.
[4] U. Suhuddin, S. Mironov, Y. Sato, H. Kokawa, C.-W. Lee, Acta Mater. 57 (2009) 5406–5418.
[5] V.K. Patel, S.D. Bhole, D.L. Chen, Scr. Mater. 65 (2011) 911–914.
[6] U.F.H. Suhuddin, V. Fischer, J.F. dos Santos, Scr. Mater. 68 (2013) 87–90.
[7] J. Shen, U.F.H. Suhuddin, M.E.B. Cardillo, J.F. dos Santos, Appl. Phys. Lett. 104 (2014) 191901.
[8] J. Shen, S.B.M. Lage, U.F.H. Suhuddin, C. Bolfarini, J.F. dos Santos, Metall. Mater. Trans. Phys. Metall. Mater. Sci. 49 (2018) 241–254.
[9] Z. Shen, Y. Chen, J.S.C. Hou, X. Yang, A.P. Gerlich, Sci. Technol. Weld. Join. 20 (2015) 48–57.
[10] A.H. Plaine, U.F.H. Suhuddin, C.R.M. Afonso, N.G. Alcantara, J.F. dos Santos, Mater. Des. 93 (2016) 224–231.
[11] Z. Shen, Y. Ding, J. Chen, B.S. Amirkhiz, J.Z. Wen, L. Fu, A.P. Gerlich, J. Mater. Sci. Technol. 35 (2019) 1027–1038.
[12] Z. Shen, Y. Ding, J. Chen, A.P. Gerlich, Int. J. Fatigue 92 (2016) 78–86.
[13] L.C. Campanelli, U.F.H. Suhuddin, A.Í.S. Antonialli, J.F. dos Santos, N.G. de Alcantara, C. Bolfarini, J. Mater. Process. Technol. 213 (2013) 515–521.
[14] A.A. Luo, J. Magnes. Alloys 1 (2013) 2–22.
[15] Z. Wu, R. Ahmad, B. Yin, S. Sandlöbes, W.A. Curtin, Science 359 (2018) 447–452.
[16] J.H. Hwang, A. Zargaran, G. Park, O. Lee, B.-J. Lee, N.J. Kim, J. Magnes. Alloys 9 (2021) 489–498.
[17] S. Mironov, T. Onuma, Y.S. Sato, H. Kokawa, Acta Mater. 100 (2015) 301–312.
[18] R. Xin, B. Li, A. Liao, Z. Zhou, Q. Liu, Metall. Mater. Trans. A 43 (2012) 2500–2508.
[19] A.H. Feng, Z.Y. Ma, Acta Mater. 57 (2009) 4248–4260.
[20] A. Tripathi, A. Tewari, A.K. Kanjarla, N. Srinivasan, G.M. Reddy, S.M. Zhu, J.F. Nie, R.D. Doherty, I. Samajdar, Metall. Mater. Trans. Phys. Metall. Mater. Sci. 47 (2016) 2201–2216.
[21] J. Chen, H. Fujii, Y. Sun, Y. Morisada, K. Kondoh, J. Mater, Process. Technol. 242 (2017) 117–125.
[22] X. Zeng, P. Minárik, P. Dobroň, D. Letzig, K.U. Kainer, S. Yi, Scr. Mater. 166 (2019) 53–57.
[23] B.C. Suh, J.H. Kim, J.H. Bae, J.H. Hwang, M.S. Shim, N.J. Kim, Acta Mater. 124 (2017) 268–279.
[24] B. Beausir, S. Biswas, D.I. Kim, L.S. Tóth, S. Suwas, Acta Mater. 57 (2009) 5061–5077.
[25] S.Q. Zhu, H.G. Yan, X.Z. Liao, S.J. Moody, G. Sha, Y.Z. Wu, S.P. Ringer, Acta Mater. 82 (2015) 344–355.
[26] F.R. Elsayed, N. Hort, M.A. Salgado Ordorica, K.U. Kainer, Mater. Sci. Forum 690 (2011) 65–68.
[27] A.P. Hammersley, J. Appl. Crystallogr. 49 (2016) 646–652.
[28] S.B. Yi, C.H.J. Davies, H.G. Brokmeier, R.E. Bolmaro, K.U. Kainer, J. Homeyer, Acta Mater. 54 (2006) 549–562.
[29] American Welding Society, AWS D17.2/D17.2M:2013 specification for resistance welding for aerospace applications, 2013.
[30] N. Stanford, R.K.W. Marceau, M.R. Barnett, Acta Mater 82 (2015) 447–456.
[31] B. Beausir, L.S. Tóth, K.W. Neale, Acta Mater. 55 (2007) 2695–2705.
[32] S. Mironov, Q. Yang, H. Takahashi, I. Takahashi, K. Okamoto, Y.S. Sato, H. Kokawa, Metall. Mater. Trans. A 41 (2010) 1016–1024.
[33] F.C. Liu, Z.Y. Ma, M.J. Tan, Metall. Mater. Trans. Phys. Metall. Mater. Sci. 44 (2013) 3947–3960.
[34] H. Liu, K. Ushioda, H. Fujii, Acta Mater 166 (2019) 324–334.
[35] Z. Mengran, S. Yufeng, M. Yoshiaki, U. Kohsaku, F. Hidetoshi, J. Magnes. Alloys 8 (2020) 1071–1083.
[36] C.D. Barrett, A. Imandoust, A.L. Oppedal, K. Inal, M.A. Tschopp, H. El Kadiri, Acta Mater. 128 (2017) 270–283.
[37] M.G. Jiang, C. Xu, H. Yan, G.H. Fan, T. Nakata, C.S. Lao, R.S. Chen, S. Kamado, E.H. Han, B.H. Lu, Acta Mater. 157 (2018) 53–71.
[38] A. Heidarzadeh, S. Mironov, R. Kaibyshev, G. Çam, A. Simar, A. Gerlich, F. Khodabakhshi, A. Mostafaei, D.P. Field, J.D. Robson, A. Deschamps, P.J. Withers, Prog. Mater. Sci. 117 (2021) 100752.
[39] É. Martin, J.J. Jonas, Acta Mater. 58 (2010) 4253–4266.
[40] S. Biswas, B. Beausir, L.S. Toth, S. Suwas, Acta Mater. 61 (2013) 5263–5277.
[41] E. Dogan, M.W. Vaughan, S.J. Wang, I. Karaman, G. Proust, Acta Mater. 89 (2015) 408–422.
[42] A. Beer, M. Barnett, Metall. Mater. Trans. A 38 (2007) 1856–1867.